Please cite this article in press as: Biswas and Levy, Ion-mediated effects of glycosylation on the disordered mucin domain: Insights from coarse-grained simulations, Biophysical Journal (2025), https://doi.org/10.1016/j.bpj.2025.07.021

Biophysical Journal
Article

Biophysical Society

Ion-mediated effects of glycosylation on the disordered mucin domain: Insights from coarse-grained simulations

Gargi Biswas[1] and Yaakov Levy[1,*]
[1]Department of Chemical and Structural Biology, Weizmann Institute of Science, Rehovot, Israel

ABSTRACT Mucins are essential glycoproteins that form the backbone of mucus, a hydrogel protecting epithelial surfaces throughout the body. Their biophysical properties are governed by the densely glycosylated and highly disordered proline-threonine-serine (PTS) mucin domain, which becomes negatively charged by the addition of terminal sialic acid and sulfate groups to its glycans. The properties of mucins are further modulated by their interactions with cations, particularly sodium and calcium, which influence mucus expansion and viscoelasticity. Alterations in mucin glycosylation patterns or cation interactions contribute to the development of various pathological conditions. Modulating mucin's functional relationships to ameliorate these conditions requires first obtaining a detailed understanding of its structure; however, the large size, extensive disorder, and polymeric nature of mucins present significant challenges to their structural characterization. Here, we employed a coarse-grained modeling approach to investigate the effects of glycosylation, glycan charge, and salt concentration on mucin PTS organization. Using two different glycan structures, we explored how their interactions with monovalent (Na^+) and divalent (Ca^{2+}) cations affect the structural organization and ionic interactions of the PTS region. Our findings revealed that the presence of cations promoted tighter mucin conformations, with divalent cations inducing greater structural compaction than monovalent cations, consistently with their greater charge shielding efficacy. Higher glycosylation levels and greater glycan charge densities enhance local glycan clustering and overall PTS structural expansion through their effects on cation binding and electrostatic repulsion. Furthermore, we examined the diffusion of charged peptides within mucin, demonstrating that peptide net charge affects both penetration and mobility. This study provides a comprehensive understanding of the structural organization and ionic interactions of mucin PTS, offering valuable insights into the molecular basis of mucin's protective properties and its role in health and disease.

SIGNIFICANCE The biophysical properties of mucin proteins, which form hydrogels that protect epithelial surfaces, are largely determined by their extensive intrinsically disordered regions (IDRs). These regions undergo O-linked glycosylation, producing highly negatively charged polymers. Using coarse-grained molecular dynamics simulations of various designed variants of these long IDRs, we quantify how glycosylation levels, glycan composition, salt type, and salt concentration influence mucin structure. Interactions with monovalent (Na^+) and divalent (Ca^{2+}) cations modulate the structural organization of the IDRs, promoting more compact mucin conformations. The interplay between glycosylation and ionic conditions provides molecular insights into mucus-related pathological conditions.

INTRODUCTION

Mucus is a hydrogel that serves to protect epithelial surfaces in areas not covered by skin (1). It lines the respiratory, gastrointestinal, reproductive, and oculo-rhino-otolaryngological tracts in the human body and fulfills a range of functions, including maintaining hydration, facilitating the passage of molecules across the epithelium, acting as a barrier against pathogens and harmful substances, and enabling nutrient exchange with the epithelium (2,3). Mucus consists of water, mucin proteins, salts, lipids (such as fatty acids, phospholipids, and cholesterol), as well as immunological components (such as immunoglobulins, growth factors, defensins, and trefoil factors) (4,5). Central to mucus composition are mucin proteins, which are large extracellular glycoproteins ranging in size from 0.5 to 20 MDa and encoded by the *MUC* gene family (6). This family encodes up to 21 known proteins, which are classified as either

Submitted February 9, 2025, and accepted for publication July 18, 2025.
*Correspondence: koby.levy@weizmann.ac.il
Editor: Chris Neale.
https://doi.org/10.1016/j.bpj.2025.07.021

Please cite this article in press as: Biswas and Levy, Ion-mediated effects of glycosylation on the disordered mucin domain: Insights from coarse-grained simulations, Biophysical Journal (2025), https://doi.org/10.1016/j.bpj.2025.07.021

secreted or membrane-bound mucins (1,6). Although hundreds of proteins have been identified in mucus gel, its fundamental properties, such as viscoelasticity, hydration, selective permeability, and density, are mainly governed by mucin proteins (7).

The biophysical properties of mucin proteins can be attributed to two key features, which are shared by both membrane-bound and secreted mucins; namely, the presence of a large central disordered region, and the occurrence of high-density O-linked glycosylation within this region. At the core of both membrane-bound and secreted mucins is a large, disordered region known as the PTS domain, so called because it is characterized by a variable number of tandem repeats enriched in proline, threonine, and serine resides (3,4,6). The length of the tandem repeats can vary in the range of 7–135 amino acids, and their number can vary in the range of 10–500 (8). The sequence and length of the PTS domain are unique to each mucin and are not conserved across mucins between species (9). The length of the disordered region can vary widely, with approximately 3200 amino acids in MUC2, 4300 in MUC6, 6500 in MUC19, and up to 12,000 amino acids in MUC16, which has the largest PTS domain identified to date (7,9).

The hydroxyl groups of the serine and threonine residues in the mucin PTS domain serve as sites for extensive O-glycosylation, with glycan sugar chains added to 50–100% of these sites depending on the type of cell, its physiological state, and the glycosyltransferases it expresses (9). Glycosyltransferases attach glycan chains to these glycosylation sites, with each chain consisting of 2–20 monosaccharide units (4). Mucins can contain over 200 distinct glycan structures (2), with carbohydrates accounting for around 50–80% of their dry mass (1). These oligosaccharide chains can be linear or moderately branched and commonly contain sugars, such as N-acetyl galactosamine (GalNAc), N-acetylglucosamine (GlcNAc), fucose (Fuc), and galactose (Gal) (4). Although the charge on these sugars is typically neutral, the terminal sugars in most glycan chains are often negatively charged (e.g., sialic acid [N-acetylneuraminic acid, Neu5Ac]) or they undergo sulfation, which contributes additional negative charge (6,10). Overall, the abundance of Neu5Ac and sulfate groups causes mucins to function as a negatively charged polyelectrolyte gel (5,10,11).

Another key feature, specific to gel-forming secreted mucins, is their polymeric nature (12). Whereas membrane-bound mucins are typically either dimeric or monomeric, secreted mucins form large polymers (6,9). At their C- and N-termini, these mucins possess structured domains, which are rich in cysteine residues and are essential for head-to-head, tail-to-tail multimer assembly through the formation of disulfide bonds in these regions (1,13). Following its synthesis in the membrane-bound ribosomes of the rough endoplasmic reticulum, the protein core of secreted mucins is transported to the endoplasmic reticulum lumen, where dimerization of the nascent polypeptide chain occurs (4,14). The dimerized molecules are then transported to the Golgi apparatus (4,6). In the cis and medial Golgi, O-glycosylation of the PTS takes place by various glycosyltransferases (15). Following this, the glycosylated mucin dimers undergo further polymerization and are packaged in the *trans*-Golgi (16) into secretory granules of <1 μm (4). Notably, when polymeric mucin is secreted, its width can span several hundred micrometers, but it is compactly packaged into micrometer-sized vesicles. The initial organization of mucin and its subsequent rearrangement and expansion are achieved elegantly in a pH- and calcium-dependent manner (4,17,18). Evidence indicates that calcium ions neutralize and cross-link mucin polymers, causing the volume of the mucin gel to collapse 100- to 300-fold (4). During secretion, when the vesicle is exposed to the extracellular environment in which sodium ions largely replace calcium ions, triggering the rapid expansion of the mucin gel in response to a combination of the Donnan potential (19) and electrostatic repulsion between the deshielded mucin charges (4,5).

The concentrations of sodium and calcium ions play a significant role in determining the structural and functional properties of mucin gels (11,20–23). Numerous experiments have highlighted the intriguing impact of salt concentration on regulating properties such as the density, viscosity, and porosity of mucin gels (11,21–27). Thus, maintaining a regulated ionic balance within the mucus barrier is very important and increasing the calcium concentration of the extracellular milieu can dramatically hinder mucin expansion and mucus swelling (4,25). Defective mucus swelling as a result of the calcium ion not properly dislodging from the mucus matrix, even when it is in the extracellular milieu, is known to underlie some of the most severe pulmonary pathologies, including chronic obstructive pulmonary disease, cystic fibrosis, and asthma (10,25,28,29). Furthermore, local salt concentration together with local pH supports the formation of varied mucus topologies that are adapted at different parts of human body. In the gastrointestinal tract, for example, since mucus is exposed to a large volume of solvent, the mucus gel preserves a tight protective molecular mesh, whereas in the respiratory tract, mucus forms a less dense and more porous protective layer (5).

Not only salt, but also glycan quantity, length, and charge significantly influence mucin's physical and functional characteristics (30,31). Alterations to the degree of glycosylation and glycan charge have been noted in several diseases and physical conditions (32–36). For instance, in ulcerative colitis, there is a shift toward smaller glycans and reduced sulfation, which is associated with inflammation (32). In cystic fibrosis patients, the sugar chains are shorter and contain a higher number of sialic acids compared with those of healthy individuals (32). Inflammatory bowel disease patients show a reduced degree of glycosylation in their intestinal mucus, possibly leading to a compromised inner mucus layer that increases bacterial contact with the epithelium,

Please cite this article in press as: Biswas and Levy, Ion-mediated effects of glycosylation on the disordered mucin domain: Insights from coarse-grained simulations, Biophysical Journal (2025), https://doi.org/10.1016/j.bpj.2025.07.021

which may trigger inflammation (33,34). Abnormal glycosylation is also associated with tumor development (36). Modifications in glycosylation are noted for different physiological states as well, for example, cervical mucin MUC5B shows a higher degree of glycosylation and longer glycan chains during ovulation, followed by a reduction in the degree of glycosylation before and after the fertile period (35). Thus, understanding the effects of glycosylation and negatively charged sugar-cation interactions on the structural organization of mucin has significant therapeutic potential.

Previous computational efforts employed mathematical models and numerical simulations to explore equilibrium calcium binding, viscoelastic properties, and the dynamic behavior of mucin-like polyelectrolyte gels, yet these approaches were unable to provide structural insights (37,38). Similarly, mesoscopic coarse-grained (CG) modeling and simulations have been employed to study the structural (39,40), thermodynamic (41), and viscoelastic properties (42) of mucin gels, however, they could not capture the effect of electrostatic interactions and, specifically, of detailed glycan-cation interactions. Furthermore, studies examining the impact of glycosylation on mucin PTS at an atomic resolution have been limited to small fragments of the mucin's ordered domain or of the PTS region (43,44), because simulating the entire PTS or a mucin polymer comprising a few monomers is computationally intensive. This work aimed to address these limitations and provide a thorough understanding of mucin's structural organization and of glycan-cation interactions in both the secretion and presecretion stages, and to thereby bridge the gap between experimental observations (18–22,45–48) and computational modeling.

In this study, we developed a CG model of the glycosylated disordered PTS mucin domain to investigate the effects of the degree of glycosylation, glycan type, salt concentration, and salt type on the structural organization of the PTS domain and its interactions. To develop this model, we utilized the PTS sequence in human MUC2 and incorporated the structural assembly of its ordered domains (D1D2D3CysD1) based on PDB: 7A5O, as described in a previous study (13). For glycans, of the eight core O-glycan structures exhibited by human mucins (49), we selected core-3 and core-1 glycan chains, which are comprised of four monosaccharide units each. The chosen core-3 glycan, commonly found in colon mucin (50,51), bears a single sialic acid (NeuAc2-3Gal1-3/4GlcNAc1-6GalNAc1-O-Ser/Thr) and the motif (NeuAc2-3Gal1-3/4GlcNAc), known as the Sd^a antigen (Fig. 1 *A*). The selected core-1 glycan is the most prevalent in humans. Known as the ST antigen (49) it bears two sialic acids (Neu5Ac(α2-3)Gal(β1-3)[Neu5Ac(α2-6)]+/GalNAc(α1)-O-Ser/Thr, Fig. 1 *B*). The selection of these two glycans, which have the same number of monosaccharide units but differing numbers of negatively charged sialic acids, allowed us to explore the impact of varying negative charge densities on the behavior of sugar chains. To examine the influence of cations, we explicitly modeled monovalent sodium and divalent calcium ions. This approach enabled us to conduct an in-depth study of the interplay between mucin glycans and ionic environments. By utilizing a CG model, we overcame the computational limitations of all-atom simulations for a protein of this size and complexity.

MATERIALS AND METHODS

A CG model for glycosylated PTS

To develop an appropriate CG model for glycosylated PTS, all-atom molecular dynamics simulations were first conducted. The structure of a small PTS fragment comprising 20 amino acids with the sequence TTTVTP TPTPTGTQTPTTTP (derived from UniProt ID: Q02817 (52) of human MUC2, spanning residues 1993–2012 and located within the disordered PTS domain) was constructed using the "fab" module of PyMOL (53) (version 2.5.2). This fragment contained 12 potential glycosylation sites, all on threonine residues, highlighted in green in Fig. 1. Either core-3 or core-1 glycans (as shown in Fig. 1, *A* and *B*, respectively) were attached to the 12 glycosylation sites of the PTS fragment (Fig. 1, *C* and *D*) using the Glycan Reader and Modeler module from the CHARMM-GUI webserver (54). The glycosylated peptides were then solvated in a cubic simulation box filled with TIP3P water. Both glycan cores were simulated under two salt conditions: 20 mM NaCl and 10 mM $CaCl_2$. Force field parameters were obtained from the CHARMM-36m (55) force field, and energy minimization and production simulations were carried out using GROMACS 2022.6 at 300 K. The simulation parameters are further detailed in Table S1.

The CG model for glycosylated PTS was constructed by representing each amino acid and monosaccharide glycan unit as a single bead positioned at the locations of the C_α and C_1 atoms, respectively. A similar approach to modeling glycans has been used previously (56). Charged beads for amino acids and glycans were assigned scaled charges, reduced by a factor of 0.9 to align with the ionic charges (see a CG model for explicit ions). The glycan model, illustrated in Fig. 1, *A* and *B*, included two types of beads: negatively charged sugar beads and neutral sugar beads. In this model, the internal energy ($E(\Gamma)$) of any random conformation during the simulation trajectory is described by the following formula:

$$\mathrm{E}(\Gamma) = \mathrm{E}(\Gamma)_{\mathrm{Bonded}} + \mathrm{E}(\Gamma)_{\mathrm{Non-bonded}} \quad (1)$$

The bonded terms involve three types of interactions as follows:

$$\mathrm{E}(\Gamma)_{\mathrm{Bonded}} = \mathrm{E}(\Gamma)_{\mathrm{bonds}} + \mathrm{E}(\Gamma)_{\mathrm{angles}} + \mathrm{E}(\Gamma)_{\mathrm{dihedrals}} \quad (2)$$

where, each individual term is represented as follows:

$$\mathrm{E}(\Gamma)_{\mathrm{bonds}} = \sum_{\mathrm{bonds}} \frac{1}{2} \mathrm{K}_{\mathrm{bonds}} \left(\mathrm{b}_{\mathrm{ij}} - \mathrm{b}^0_{\mathrm{ij}}\right)^2 \quad (3)$$

$$\mathrm{E}(\Gamma)_{\mathrm{angles}} = \sum_{\mathrm{angles}} \frac{1}{2} \mathrm{K}_{\mathrm{angles}} \left(\theta_{\mathrm{ijk}} - \theta^0_{\mathrm{ijk}}\right)^2 \quad (4)$$

$$\mathrm{E}(\Gamma)_{\mathrm{dihedrals}} = \sum_{\mathrm{dihedrals}} \frac{1}{2} \mathrm{K}_{\mathrm{dihedrals}} \left[1 - \cos\left(\phi_{\mathrm{ijkl}} - \phi^0_{\mathrm{ijkl}}\right) + \frac{1}{2}\cos 3\left(\Phi_{\mathrm{ijkl}} - \Phi^0_{\mathrm{ijkl}}\right)\right] \quad (5)$$

Here, $\mathrm{E}(\Gamma)_{\mathrm{bonds}}$ represents the potential for bonded interactions, where b_{ij} is the distance between any two bonded beads, and $\mathrm{b}^0_{\mathrm{ij}}$ is their equilibrium

Please cite this article in press as: Biswas and Levy, Ion-mediated effects of glycosylation on the disordered mucin domain: Insights from coarse-grained simulations, Biophysical Journal (2025), https://doi.org/10.1016/j.bpj.2025.07.021

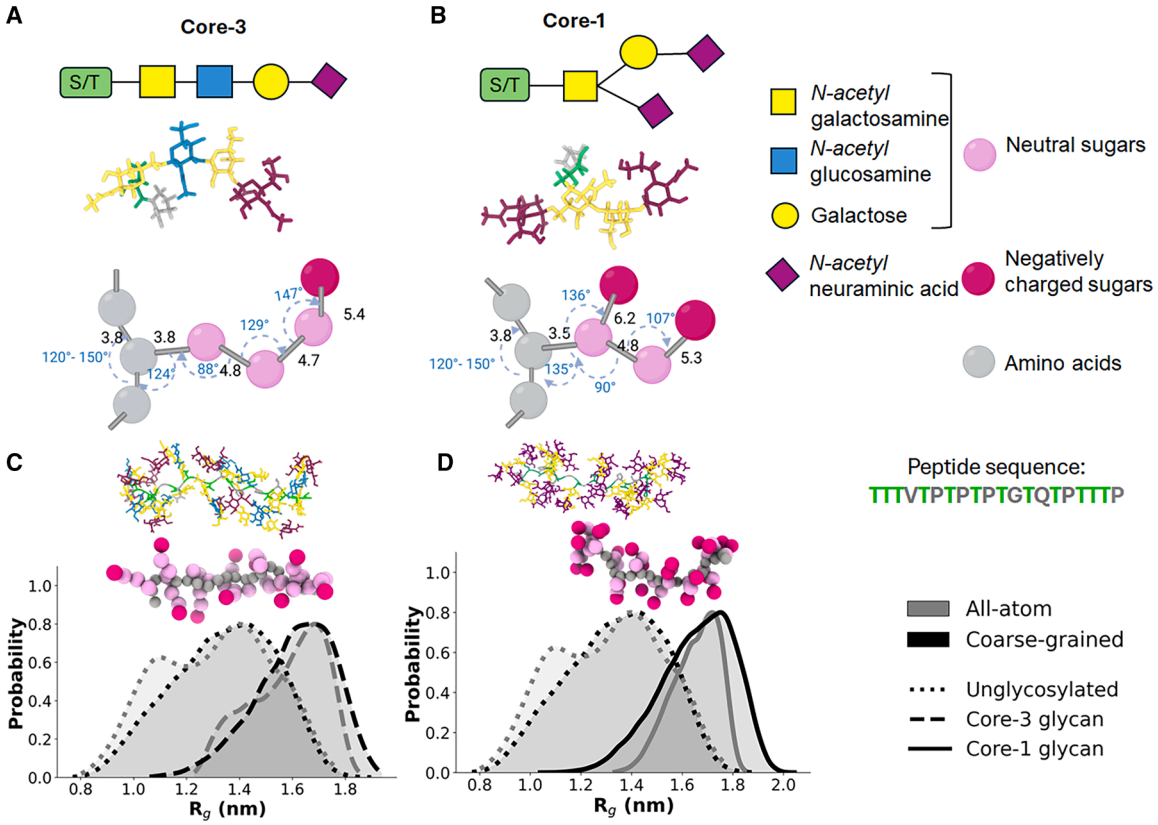

FIGURE 1 CG modeling of glycosylated PTS. (*A* and *B*) The structures of the two glycans utilized in this study: (*A*) the core-3 glycan chain, with sequence Neu5Ac(α2-3)Gal(β1-4)GlcNAc(β1-3)GalNAc(α1)-O-Ser/Thr and (*B*) the core-1 glycan chain, with sequence Neu5Ac(α2-3)Gal(β1-3)[Neu5Ac(α2-6)]+/GalNAc(α1)-O-Ser/Thr. The top panel shows the structures of the glycans as per the symbol nomenclature for glycans, which assigns a specific shape and color to each class of monosaccharide glycan units. The middle and bottom panels show all-atom ball-and-stick models and CG models, respectively, of each glycan, as per the color key to the right of (*B*). (*C* and *D*) Comparisons of the radius of gyration (R_g) of the short PTS fragment used in this study as determined using an all-atom molecular dynamics model and the CG model (*gray and black lines* in the plots, respectively). The PTS fragment, which spans residues 1993–2012 of human MUC2 (UniProt ID: Q02817), is shown glycosylated with: (*C*) core-3 glycans or (*D*) core-1 glycans. The dotted lines indicate the R_g of unglycosylated form, while the dashed and solid lines indicate the R_g of the peptide glycosylated with core-3 and core-1 glycan, respectively. Representative structures of the glycosylated peptide from all-atom and CG simulation are shown. The 19-amino-acid sequence of the PTS fragment is shown on the right, with the 12 potential glycosylation sites indicated in green.

distance. The term $E(\Gamma)_{angles}$ describes the angular potential, where any three consecutive beads interact through this potential; θ_{ijk} and θ^0_{ijk} represent the angle and the equilibrium angle between the three beads, respectively. The third term $E(\Gamma)_{dihedrals}$ accounts for the dihedral potential involving any four consecutive beads, where ϕ_{ijkl} is the dihedral angle at a given point, and ϕ^0_{ijkl} is the equilibrium dihedral angle.

We set the value for the bonded potential (K_{bonds}) to 20,000 kJ/mol and the value for the angular potential (K_{angles}) is set to 40 kJ/mol, as defined in the SMOG-based models (57). However, unlike in the SMOG models, the mass of each amino acid and glycan bead is their mass in atomic mass units and the simulation temperature is maintained at 300 K to ensure consistency with the all-atom simulation. For interactions involving only amino acid beads, the equilibrium bond length (b^0_{ij}) is set to 3.8 Å, and the equilibrium angle (θ^0_{ijk}) is set to various values between 120 and 150°. When glycan beads are involved, the equilibrium bond and angle parameters are assigned different values, as detailed by the lower ball-and-stick structures in Fig. 1, *A* and *B*. The bond and angles parameters for amino acid beads are taken from SMOG-based models, while the bond and angle parameters for glycans are obtained from the equilibrium bond and angle values among C_1/C_α atoms obtained from the all-atom structures generated by CHARMM-GUI webserver which utilizes CHARMM36 additive carbohydrate force field (58).

This model treats the glycosylated peptide as a flexible polymer, and therefore no dihedral potential is applied to the dihedrals associated with the glycan beads or to the majority of the amino acid beads. However, the presence of a significant number of proline residues introduces rigidity to the polymer, which is modeled by incorporating dihedral angles and potentials based on a previously established method (59).

Beads separated by more than three bonds interact via one or more types of nonbonded interactions, as described by $E(\Gamma)_{Non-bonded}$ in Eq. 1, the nonbonded interaction term also involves three kinds of interactions as follows:

$$E(\Gamma)_{Non-bonded} = E(\Gamma)_{Electrostatic} + E(\Gamma)_{Repulsion} + E(\Gamma)_{Contacts} \quad (6)$$

Charged beads interact through Coulomb interactions, represented by the $E(\Gamma)_{Electrostatic}$, which can be written as,

$$E(\Gamma)_{Electrostatic} = \frac{1}{4\pi\varepsilon_0}\sum_{i,j}\frac{q_i q_j}{\varepsilon_r r_{ij}} \quad (7)$$

where q_i and q_j denote the charges of the respective beads; r_{ij} is the distance between them; the electric conversion factor, $\frac{1}{4\pi\varepsilon_0}$, is

Please cite this article in press as: Biswas and Levy, Ion-mediated effects of glycosylation on the disordered mucin domain: Insights from coarse-grained simulations, Biophysical Journal (2025), https://doi.org/10.1016/j.bpj.2025.07.021

138.94 kJ mol^{-1} nm e^{-2}; and the relative permittivity of the medium (ε_r) is set to 78.0, corresponding to the permittivity of water (60). Now, any pair of beads, whether charged or uncharged, that does not interact via attractive potential, interacts via $E(\Gamma)_{Repulsion}$, which accounts for purely repulsive interactions, and can be expressed as,

$$E(\Gamma)_{Repulsion} = \sum_{i \neq j} \varepsilon_{ij}^{rep} \left(\frac{\sigma_{ij}}{r_{ij}} \right)^{12} \quad (8)$$

Here, the collision diameter (σ_{ij}) is calculated as $\sigma_{ij} = \frac{(\sigma_i + \sigma_j)}{2}$ and is set to 4 Å for amino acid beads and 6 Å for glycan beads (56). The ε_{ij}^{rep} term represents the depth of the potential, which is set to 1 kJ/mol (61). If a pair of beads interact through an additional attractive potential, this interaction is described by $E(\Gamma)_{Contacts}$, which can be expressed as,

$$E(\Gamma)_{Contacts} = \sum_{i \neq j} 4\, \varepsilon_{ij}^{contacts} \left[\left(\frac{\sigma_{ij}}{r_{ij}} \right)^{12} - \left(\frac{\sigma_{ij}}{r_{ij}} \right)^{6} \right] \quad (9)$$

Here, σ_{ij} and ε_{ij} retain their previously defined meanings as Eq. 8, with $\varepsilon_{ij}^{contacts}$ scaled to different values for specific pairs, as discussed later.

We evaluated the accuracy of the CG model against that of the all-atom model by comparing the size of the modeled PTS fragment, in terms of its structure and radius of gyration (R_g), as calculated from simulations using each model. Separate comparisons of the molecular structures and R_g values were made for the PTS peptide fragment glycosylated with core-3 glycan (Fig. 1 *C*) and core-1 glycan (Fig. 1 *D*). As shown in Fig. 1, *C* and *D*, the R_g of the unglycosylated system is smaller than that of the glycosylated systems with core-1 or core-3 glycans, consistent with prior observations (44). The absolute R_g values may depend on variations in glycan size and density. To align the R_g values obtained from the CG simulations with those obtained from all-atom simulations, we carefully tuned the bead sizes, equilibrium angles for angular potentials, and negatively charged sugar-cation interactions. Electrostatic interactions were treated using the Coulomb cutoff scheme with a cutoff distance of 3.0 nm, and a relative dielectric constant of 78 was employed to account for the screening effect of the implicit solvent as described earlier. To tune the modeled negatively charged sugar-cation interactions, we examined how the density (g) and number (n) of cationic particles varied as a function of their distance from the glycan sugars, which we took as our reference particles. To that end, we calculated the radial distribution function (62) (g(r)) and radial cumulative coordination numbers (63) (n(r)) of cations Ca^{2+} and Na^{+} around negatively charged sugar beads using the CG and all-atom models and aligned the former with the latter. To align the values of g(r) and n(r) from the CG model with those from the all-atom simulations, an additional attractive potential, represented by a Lennard-Jones interaction (Eq. 9), was introduced for negatively charged sugar-Ca^{2+} and sugar-Na^{+} pairs (Fig. S1). Details of these interaction parameters are provided in Table S2. For interactions between amino acid beads, Lennard-Jones interactions were implemented between all residues of the PTS fragment. The value of the energetic strength ($\varepsilon_{ij}^{contacts}$) was adopted from the Mpipi models, which are particularly effective for intrinsically disordered regions, as previously demonstrated (64). In addition to modeling negatively charged sugar-cation interactions, cation-anion interactions within the salt were also incorporated, as described in the next section.

A CG model for explicit ions

The CG model employed in this study treats the water molecules as implicit solvent, while the cations and anions present in the solvent have been treated explicitly. The implicit treatment of water molecules significantly reduced computational cost while retaining the essential screening effects of the solvent. On the other hand, explicit treatment of ions can capture their localized binding which can be critical for understanding mucin's structural dynamics and phase behavior. Since the model does not include explicit water molecules, the parameters for the explicit cations and anions utilized in this work required calibration. To achieve this, the CG simulations of glycosylated PTS peptide fragments were compared with those obtained from all-atom simulations of the same systems. Two separate all-atom simulation systems were constructed using the CHARMM-GUI webserver (65) (https://www.charmm-gui.org/): one containing 20 mM NaCl and the other with 10 mM $CaCl_2$, in both cases solvated with TIP3P water (66). Equilibration and production simulations were conducted using GROMACS-2022.6 (67) at 300 K for 50 ns. The simulation parameters are detailed in Table S3.

To correctly represent the strength of interactions between the cations (i.e., Na^{+} and Ca^{2+}) and the anions (i.e., Cl^{-}) in the CG model, NaCl and $CaCl_2$ were simulated using both the atomistic and CG models. In the CG model, the simulation box was populated exclusively by charged beads representing cations and anions. The number of cations and anions, as well as the box size, were set to match those of the all-atom simulations for 20 mM NaCl and 10 mM $CaCl_2$ solvated with TIP3P water. The interaction parameters for Ca^{2+}-Cl^{-} and Na^{+}-Cl^{-} ion pairs were compared by aligning g(r) and n(r) from the CG simulations with those from the all-atom model, as illustrated in Fig. S2. To match the radial distribution functions from the CG simulations with those from the all-atom model, a Lennard-Jones potential (62) was introduced between oppositely charged ions, with their respective charges screened by a factor of 0.9. This attractive potential was introduced in addition to the electrostatic potential energy, which is an acceptable method in explicit ion modeling (68–70). The parameters for the Lennard-Jones interactions utilized here are detailed in Table S4.

Modeling the phase separation behavior of glycosylated PTS polymers

To understand the phase separation behavior of the glycosylated PTS, we designed 2 types of simulation systems: 50 PTS polymers (each of 20 residues, peptides as described in a CG model for glycosylated PTS) glycosylated with either core-3 or core-1 (Fig. S3). Both systems were charge-neutralized by adding either monovalent or divalent cations, and additional explicit cations and anions were introduced to achieve specific salt concentrations. Each system was studied under two salt conditions: 20 mM NaCl and 10 mM $CaCl_2$. The number of cations and anions used in each setup is detailed in Table S5. Simulations were performed at various temperatures for both systems.

Modeling the effect of salt concentration and glycosylation on the glycosylated PTS polymer

In this study, we constructed a glycosylated PTS polymer filament by linking four identical PTS fragments, each consisting of 2500 amino acids (Fig. S4, *A* and *B*). These PTS fragments were derived from the human MUC2 protein (UniProt ID: Q02817) and spanned residues 1834–4334. Notably, 58% of the residues in this PTS fragment were threonine or serine, which can serve as potential glycosylation sites, whereas 21% were proline and 9% are hydrophobic residues, such as valine or isoleucine. When mucin is secreted as a polymer, each mucin monomer forms noncovalent pairings: its N-terminal ordered domain pairs with the N-terminal ordered domain of another monomer, and its C-terminal pairs with the C-terminal of a different monomer (Fig. S4 *A*). This arrangement creates a continuous filament of sequentially (head-to-head, tail-to-tail) linked mucin monomers. In this study, we constructed a polymer filament consisting of only glycosylated PTS fragments that were sequentially linked in a manner similar to that found in secreted mucin PTS (Fig. S4 *A*).

Various proportions of potential glycosylation sites are actually glycosylated in the naturally occurring PTS mucin domain. We therefore

Please cite this article in press as: Biswas and Levy, Ion-mediated effects of glycosylation on the disordered mucin domain: Insights from coarse-grained simulations, Biophysical Journal (2025), https://doi.org/10.1016/j.bpj.2025.07.021

modeled two degrees of glycosylation: 40 and 80%. For 40% glycosylation, we attached either core-1 or core-3 glycans to a random selection of 40% of the glycosylation sites, whereas for 80% glycosylation, the relevant core was attached to a random selection of 80% of these sites (Fig. S4, *C* and *D*). This approach allowed us to construct four independent systems, each combining a specific glycan type (core-1 or core-3) with a specific degree of glycosylation (40 or 80%). To simulate different salt conditions, cations were added to achieve charge neutralization, with extra cations and anions subsequently added to achieve the desired salt concentrations. We examined four salt conditions: 10 and 20 mM NaCl, as well as 5 and 10 mM $CaCl_2$ to compare the structure of glycosylated mucin PTS under monovalent and divalent ion environments. Additionally, a control system containing no added salt was also studied. This resulted in a total of 5 salt conditions for each of the 4 systems, yielding 20 independent systems in total. To further investigate physiological salt conditions, 40 and 80% glycosylated systems containing core-1 glycans were also simulated at 150 mM NaCl, yielding a total of 22 independent simulation systems. Details of these simulation setups are provided in Table S6.

Modeling peptide diffusion through the glycosylated PTS polymeric assembly

For the secreted mucin model, we used the system described earlier that includes a 10,000 residue PTS chain comprised of 4 identical fragments each consisting of 2500 amino acid residues. To study peptide diffusion through the PTS, we utilized PTS glycosylated to 40% with either core-3 or core-1 glycans. To model peptide diffusion, we selected therapeutic-sized peptides consisting of 20 amino acids each, with 100 identical peptides included in each system. These peptides were randomly distributed in close proximity to the PTS assembly, as illustrated in Fig. S5. For the simulations, we focused on 20 mM NaCl conditions for all systems. Five types of peptides with net charges of +10, +7, +4, −7, and −10 (detailed in diffusion of peptides through an assembly of glycosylated PTS polymers) were studied on the basis of their experimental characterization (71) to include a range of peptides spanning different behaviors. Their diffusion through the glycosylated PTS polymer was analyzed during the simulations by calculating the mean-square displacement (*MSD*) of the center of mass (COM) of each peptide, from which the diffusion coefficient was obtained. The values for the *MSD* of the COM were calculated for each peptide using the equation:

$$MSD\ (\tau) = \sum_{i=t_0}^{t-\tau} \frac{(r_{i+\tau} - r_i)^2}{(t-\tau)} = 2dD\tau \qquad (10)$$

where r is the position of the protein COM, t is the number of time steps measured, and τ is the measurement window ranging from t_0 to t. The slope of the *MSD* is $2dD$, where d is the dimensionality of diffusion and D is the diffusion coefficient. We first identified peptides that remained inside mucin for at least 500 consecutive frames. For these periods, the *MSD* was calculated over time lags ranging from 1 to 200 frames. In addition to calculating the diffusion coefficient, the probability of peptide recruitment into the glycosylated PTS polymer was also evaluated. A peptide was considered recruited into the glycosylated PTS if its COM was within 15 Å of any PTS bead. The recruitment probability was defined as the ratio of the total number of time frames during which a peptide is recruited to the total number of time frames analyzed. The likelihood of these interactions occurring throughout the simulation, referred to as the recruitment probability, indicates whether the peptide has entered the mucin matrix. Furthermore, the electrostatic interaction energy between the peptides and the PTS polymers was calculated from the simulation. The recruitment probability obtained from the CG simulations was compared with the penetration depth measured experimentally and reflects the penetration of peptides in a microfluidic polydimethylsiloxane device containing 1.5% (w/v) purified MUC5AC mucin over a 10-min period (71).

Modeling the multimer assembly of full-length MUC2 monomers

The structural organization of MUC2 monomers differs between their presecretion and secretion states. As previously described, during secretion, MUC2 monomers link sequentially to form a chain-like structure. In contrast, in the presecretion state, monomers first form dimers, which then assemble into larger complexes. When a MUC2 filament assembles before secretion, two monomers first form a head-to-head, tail-to-tail closed dimer through noncovalent pairings at their respective C- and N-terminal domains (Fig. S6 *A*). In this presecretion assembly, all the D1, D2, and D3 regions of the head domain remain intact, with the D1 and D2 being released only upon MUC2 secretion (Fig. S6, *A* and *B*). Once the dimer is formed in the presecretion assembly, multiple dimer heads interact through noncovalent bonds to create a compact filament. Meanwhile, the PTS regions and dimer tails loosely assemble around the filament, as depicted in Fig. S6 *B*. In this study, we modeled a mucin head filament consisting of eight mucin monomers, based on the earlier work (13) (Fig. S6 *C*). The PTS domain was glycosylated to varying degrees (40 and 80%) using core-1 and core-3 glycans and placed in two different salt conditions: 20 mM NaCl and 10 mM $CaCl_2$. Additionally, as a control, we simulated the system in the absence of salt. This setup allowed us to perform 12 independent simulations, combining 2 glycan types (core-1 and core-3), 2 glycosylation levels (40 and 80%), and 3 salt conditions (no salt, 20 mM NaCl and 10 mM $CaCl_2$).

RESULTS AND DISCUSSION

Ion-mediated condensation of glycosylated PTS

We utilized our CG model of a glycosylated PTS peptide polymer bearing either core-3 or core-1 glycans to investigate whether the presence of cations (monovalent or divalent) drives the polyanionic polymer to form a biomolecular condensate and, if so, under what conditions condensate formation optimally occurs. Interestingly, despite the polymers being negatively charged, biomolecular condensates with distinct clustered regions were observed at low temperatures. At higher temperatures, however, the polymers remained uniformly mixed. The temperature above which phase separation no longer occurs is referred to as the critical temperature (Tc). The relationship between temperature and polymer density is depicted in the phase diagrams shown in Fig. 2, *A* and *B*, where the temperature has been expressed in the T_C scale. Simulation snapshots at four different temperatures (Fig. 2 *D*) illustrate the phase transition: the polymers clustered into a single phase at low temperatures $0.7T_C$; however, this behavior diminished with increasing temperature, resulting in uniformly mixed polymers at high temperatures $1.2\,T_C$. This temperature-dependent behavior can be attributed to the cations shielding the negative charges on the glycans, thus facilitating phase separation. At lower temperatures, the reduced thermal energy of the glycosylated chains enhanced the effectiveness of this process, whereas at higher temperatures, the greater entropy of the cations decreases their likelihood to bind glycans and hence reduce phase separation.

The Tc of phase separation is affected by the valency of the cations interacting with the disordered PTS chain. For both types of glycans, Ca^{2+} ions yielded a higher Tc

Please cite this article in press as: Biswas and Levy, Ion-mediated effects of glycosylation on the disordered mucin domain: Insights from coarse-grained simulations, Biophysical Journal (2025), https://doi.org/10.1016/j.bpj.2025.07.021

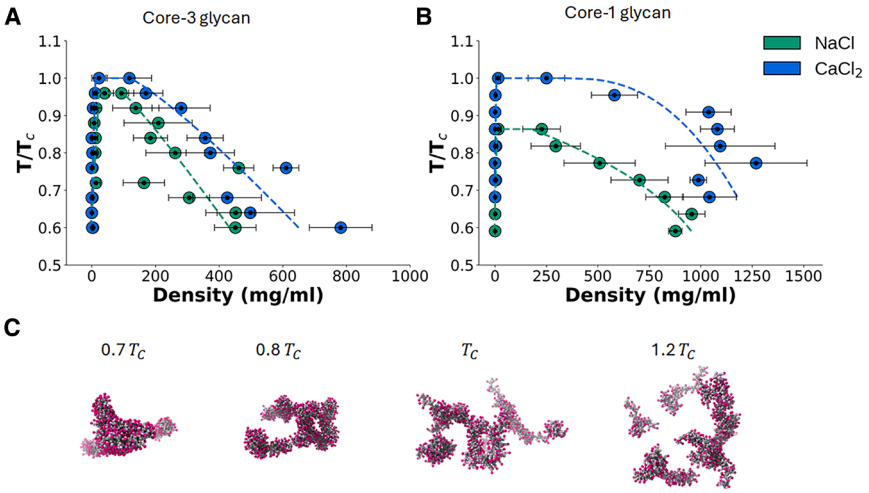

FIGURE 2 Ion-mediated condensation of glycosylated disordered PTS regions. Phase diagrams of disordered PTS glycosylated with: (*A*) core-3 glycans and (*B*) core-1 glycans simulated in the presence of two types of salt at two different concentrations, as indicated in the legend. The phase diagrams were obtained by simulating 50 copies of the PTS chain glycosylated with core-3 glycans, and repeating for PTS glycosylated with core-1 glycans. Each PTS chain consists of 20 residues (as per Fig. 1, *C* and *D*), with 100% glycosylation of their Thr residues. The temperature is expressed in the scale of T_C for corresponding $CaCl_2$ salt. (*C*) The condensation of multiple peptides into a single phase and the gradual loss of phase separation at higher temperatures are depicted using snapshots from four independent simulations conducted with core-1 glycans and $CaCl_2$ at the four temperatures shown.

compared with Na^+ ions, which reflects the stronger electrostatic interactions and bridging effects provided by divalent ions over monovalent ions (Fig. 2, *A* and *B*). Moreover, the value of T_c is also dependent on the surface charge density (σ) of the PTS polymer. Notably, the surface charge density of polymers with core-1 glycans ($\sigma = 0.38$ nm^{-2}) was higher than that of polymers with core-3 glycans ($\sigma = 0.20$ nm^{-2}). PTS chains glycosylated with core-1 glycans underwent phase separation at comparatively lower temperatures compared with those glycosylated with core-3 glycans, which can be attributed to the increased electrostatic repulsion between the polymers. This repulsion inhibited the condensation process, lowering the thermal energy threshold at which attractive forces prevailed. Although Ca^{2+} ions provide more-effective charge shielding than Na^+ ions, it appears that, for phase separation, the lower charge density core-3 system relied more on the concentration of the ions than their valency. This explains the smaller difference in Tc between Ca^{2+} and Na^+ for polymers bearing core-3 glycans compared with core-1 glycans (Fig. 2, *A* and *B*).

In addition to electrostatic interactions, networks of glycosylated disordered PTS chains are influenced by several other interactions that play a critical role in their condensation, including direct and water-mediated sugar-sugar interactions. Indeed, excluding sugar-sugar interactions produced a sharp decrease in the value of Tc (Fig. S7), which indicates that compensation for the strong electrostatic repulsive interactions between the glycans occurs not only via ion-mediated interactions but also via various other interactions (e.g., sugar-sugar and aromatic-aromatic residue interactions) whose exact strength may depend on the length and type of the glycan and on the amino acid content of the PTS sequence. Simulations were performed at various temperatures in the range of 0.6–1.0 T_C at small intervals. For peptides glycosylated with core-1 and core-3 glycans simulations are presented at temperatures corresponding to T ≈ 0.8 T_c, where the value of T_c corresponds to the value obtained from condensation with Ca^{2+}. We selected a simulation temperature of 0.8 T_C to represent conditions below the critical point, where structural fluctuations relevant to self-assembly begin to emerge. This choice is consistent with previous studies where room temperature typically corresponds to ∼0.8 T_C for similar polyelectrolytic biopolymers (72,73).

Effect of salt concentration and degree of glycosylation on PTS polymer assembly

Cations play a critical role in driving the condensation of glycosylated PTS as they mediate interactions between the negatively charged glycans. Building on this understanding, we sought to investigate how salt concentration and the degree of glycosylation may affect the structure and dynamics of a highly glycosylated, long PTS chain. Since both glycosylation levels and salt concentration are key factors in mucin dynamics, as previously mentioned, we constructed four distinct systems (see modeling the effect of salt concentration and glycosylation on the glycosylated PTS polymer) to study the effect of glycosylation and salt on secreted mucin. Fig. 3 presents representative structures from these CG simulations, which can be categorized into three distinct groups. First, in the absence of salt, the negative charges on the glycans repelled each other, leading to the most-expanded structures. Second, in the presence of NaCl, the structures became comparatively more compact, as Na^+ ions partially neutralized the negative charges on the sugars, bringing them closer together. Finally, in the presence $CaCl_2$, the effects of charge screening were significantly stronger, and the negative charges likely engaged in ion-mediated interactions, resulting in the most compact conformations across all systems. Additionally, the residence time of Ca^{2+} ions was 4.6 ± 2.4 ps, compared with 3.2 ± 2.0 ps for Na^+ ions (Fig. S8 *A*). This longer residence

Please cite this article in press as: Biswas and Levy, Ion-mediated effects of glycosylation on the disordered mucin domain: Insights from coarse-grained simulations, Biophysical Journal (2025), https://doi.org/10.1016/j.bpj.2025.07.021

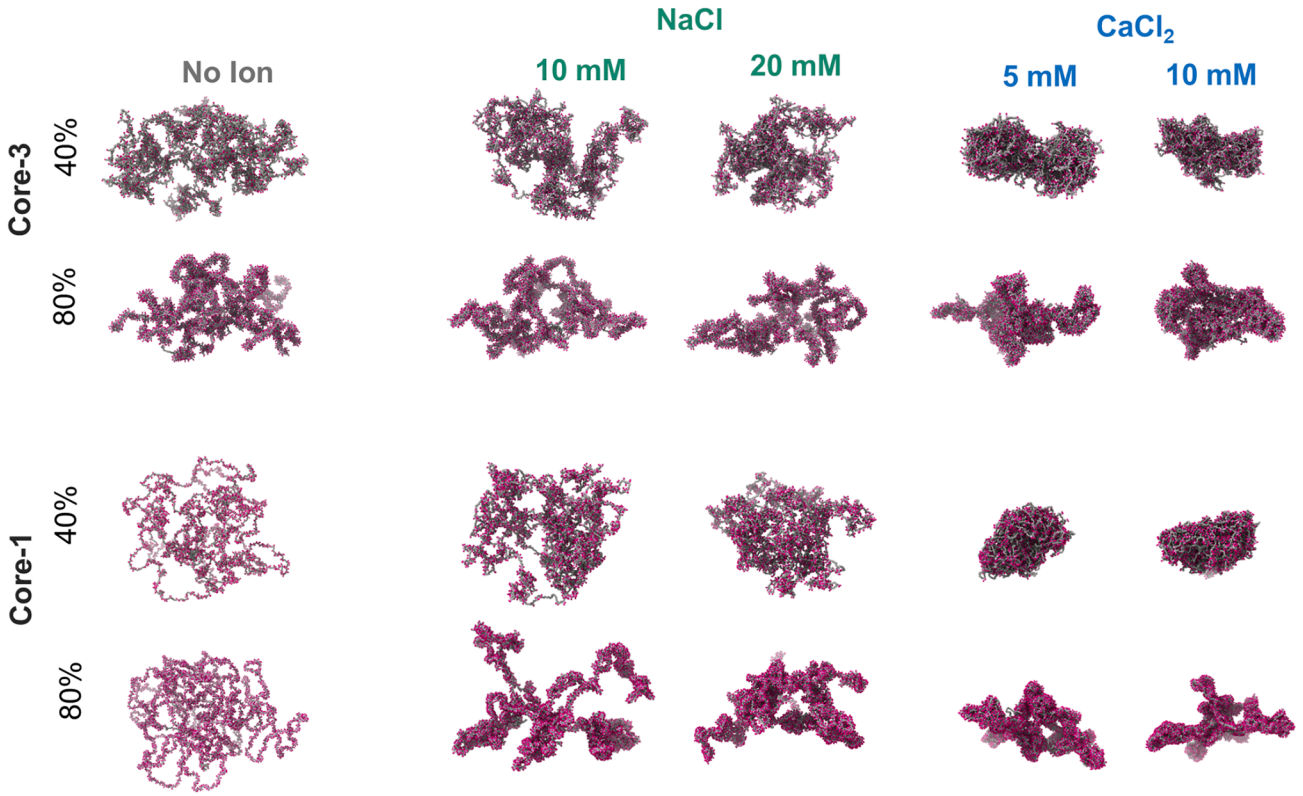

FIGURE 3 Structures of glycosylated PTS polymers under varying glycosylation and salt conditions. Representative structures of PTS polymers glycosylated with core-3 and core-1 glycans at two glycosylation levels (40 and 80%) and under four salt conditions (10 and 20 mM NaCl, 5 and 10 mM $CaCl_2$) as obtained from the CG simulations. As a control, representative snapshots from simulations undertaken in the absence of salt are also included in each case. Each simulation involved four glycosylated disordered PTS fragments, each of 2500 residues, that were connected head-to-tail to form a polymer.

time, combined with the stronger charge screening provided by Ca^{2+}, contributed to the increased structural compactness observed with $CaCl_2$.

The structure of glycosylated PTS was studied under five salt conditions: 10, 20, and 150 mM NaCl, as well as 5 and 10 mM $CaCl_2$. A greater number of cations are available for negative charge shielding at 20 and 150 mM NaCl compared with 10 mM NaCl. Consistent with this, the structures were more compact in the presence of 20 and 150 mM NaCl (Fig. 3). However, minimal differences were observed between the structures in 5 and 10 mM $CaCl_2$, suggesting that charge shielding reaches saturation at 5 mM $CaCl_2$ for this type of salt. The stronger effect of calcium ions compared with sodium ions on the compaction of glycosylated PTS is illustrated by comparing the greater effect of 10 mM $CaCl_2$ compared with 20 mM NaCl (Fig. 3). Overall, the Rg values followed the pattern: no salt >10 mM NaCl >20 mM NaCl >150 mM NaCl >5 mM $CaCl_2$ ≈ 10 mM $CaCl_2$ (Fig. 4 *A* for core-1 glycans; Fig. S8 *B* for core-3 glycans). The degree of glycosylation also had a large effect on the structural organization of the PTS. Glycosylation of 80% of sites on the PTS polymer resulted in structural elements that were more localized compared with a more globular shape for 40% glycosylation. It is likely that the high density of negatively charged glycans produced strong electrostatic repulsion that could be locally neutralized by cations, resulting in the formation of local structural elements. This mechanism can explain how the formation of clusters of smaller, denser, and more compact elements at the higher glycosylation level produces a more expanded and asymmetrical PTS structure.

The radial distribution of cations around the negatively charged sugars peaks at approximately 4.4 Å (Fig. S8 *C*), with most ions located within 5 Å of a sugar. Consequently, we defined the cutoff distance for the charge shielding effect as 5 Å from the sugar. A cation located within a 5 Å radius of any negative charge was considered to be a member of a cation-anion pair and was thus defined as a neutralized charge. We note that a cation that is within 5 Å to more than one negatively charged glycan may lead to their partial neutralization but will be counted here as neutralization. The percentage of neutralized charges across all systems is presented in Fig. 4 *B* (core-1) and Fig. S8 *D* (core-3). The percentage of neutralized charges increased as follows: 10 mM NaCl <20 mM NaCl <150 mM NaCl <5 mM $CaCl_2$ ≈ 10 mM $CaCl_2$. Interestingly, despite bearing more negatively charged glycans, systems glycosylated at 80% of sites exhibited a higher percentage of neutralized charges compared with those glycosylated at 40% of sites at the same salt concentration, as shown in Fig. 4 *B* with respect to glycosylation with core-1 glycan. This finding

Please cite this article in press as: Biswas and Levy, Ion-mediated effects of glycosylation on the disordered mucin domain: Insights from coarse-grained simulations, Biophysical Journal (2025), https://doi.org/10.1016/j.bpj.2025.07.021

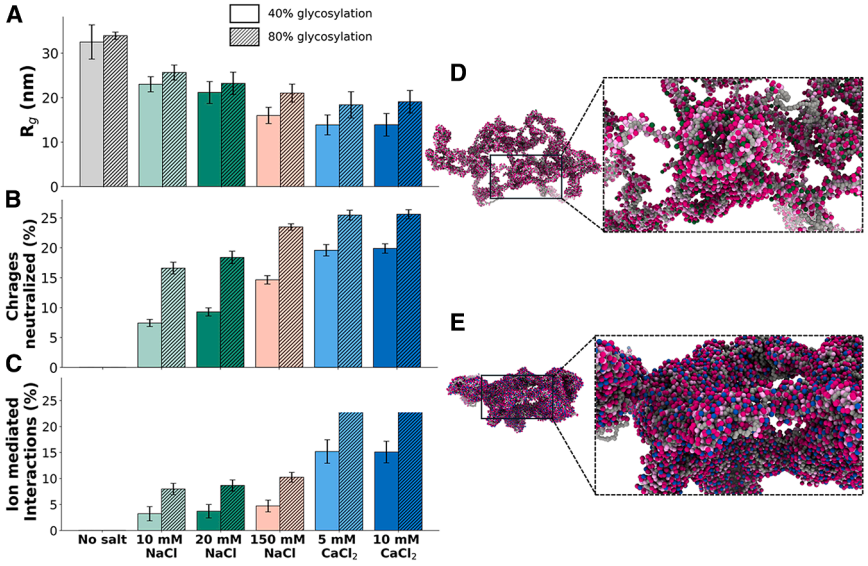

FIGURE 4 Structural analysis of glycosylated PTS polymers under varying salt and glycosylation conditions. (*A–C*) Mean radius of gyration (R_g). (*A*) Percentage of charge neutralization (*B*) and percentage of ion-mediated interactions (*C*) of the disordered PTS domain glycosylated with core-1 glycan in the presence of NaCl (*green*) or $CaCl_2$ (*blue*). Data are presented for two salt concentrations and for two glycosylation levels. (*D* and *E*) Representative structures of disordered PTS glycosylated with core-1 glycan to the 80% glycosylation level, showing adsorbed cations at 20 mM NaCl (*D*) and 10 mM $CaCl_2$ (*E*). These snapshots were taken from simulations of four copies of glycosylated PTS fragments, each comprised of 2500 amino acid residues that were connected sequentially in head-to-head, tail-to-tail. The cations are shown as green (Na^+) and blue (Ca^{2+}) spheres. Amino acid residues and monosaccharides are shown in gray and shades of pink, as per the legend of Fig. 1.

is likely due to the increased charge density at the 80% glycosylation level enhancing the ability of a single cation to neutralize multiple negative charges. Similarly, the higher charge density in core-1 glycans enabled a single cation to neutralize multiple charges at once, which can account for the higher percentage of neutralized charges in core-1 glycans compared with core-3 glycans (Figs. 4 *B* and S8 *D*). Furthermore, the variance in the atomic positions of amino acid beads along the first two principal components indicates that core-3 glycan systems exhibited greater conformational variability under both NaCl and $CaCl_2$ conditions compared with core-1 glycan systems (Fig. S9). This may be attributed to the larger number of electrostatic interactions in core-1 glycans restricting their movement within the conformational space during the simulation.

Further, the role of each type of individual cation in promoting ion-mediated interactions among the negatively charged sugar residues, have also been explored. As previously shown in Fig. 4 *B*, we quantified the number of negatively charged sugar moieties within a 5 Å radius of each Na^+ or Ca^{2+} ion—this count, denoted as C_n, represents partially or fully neutralized sugars. Building on this, we identified how many of these ions simultaneously interact with at least two distinct sugar residues within the same cut-off distance, representing potential ion-mediated interactions (I_m). To assess the extent of such interactions, we calculated the percentage of neutralized sugars involved in ion-mediated interactions as $(I_m/C_n) \times 100$, which is presented in Fig. 4 *C*. The results indicate that $CaCl_2$ promotes a higher proportion of ion-mediated interactions compared with NaCl highlighting that the Ca^{2+} effect is not only due to a greater electrostatic effect but due to its higher ability to bridge between two negatively charged sugars.

The representative structures from the CG simulations shown in Fig. 4 *C* illustrate how sodium and calcium ions distribute around negative sugar beads, effectively neutralizing their charges. Notably, the simulations showed the charge shielding effect to be more pronounced for $CaCl_2$ (*right panel*) compared with NaCl (*left panel*). This stronger shielding effect facilitates the formation of a greater number of compact local structures in the presence of $CaCl_2$. Overall, salt concentration, glycan charge, and the degree of glycosylation significantly influenced the structural organization of the glycosylated PTS polymer.

Diffusion of peptides through an assembly of glycosylated PTS polymers

Proper functioning of the glycosylated PTS mucin polymers involves pathogens, therapeutic small molecules, and peptides passaging through them. Numerous previous studies (71,74–79) suggest that the motility of particles diffusing through mucin is influenced not only by particle size, but also by particle net charge and charge distribution. Drawing inspiration from a previous study (71), we designed therapeutic peptides that varied with respect to their net charge and investigated their interaction with and diffusion through mucin (see modeling peptide diffusion through the glycosylated PTS polymeric assembly).

To obtain a detailed understanding of how net charge affects peptide diffusion through glycosylated mucin PTS, we constructed and analyzed five peptide sequences (as shown in Fig. 5 *A*) bearing various net charges (as indicated in brackets): K (+10), KF (+7), KE (+4), EF (−7), and E (−10). The relationship between the experimental penetration depth and recruitment probabilities in the presence of 20 mM NaCl is presented for mucin PTS glycosylated with core-3 glycans in Fig. 5 *B*, with the corresponding data for glycosylation with core-1 glycans shown in Fig. S10 *A*. The simulations showed that the recruitment

Please cite this article in press as: Biswas and Levy, Ion-mediated effects of glycosylation on the disordered mucin domain: Insights from coarse-grained simulations, Biophysical Journal (2025), https://doi.org/10.1016/j.bpj.2025.07.021

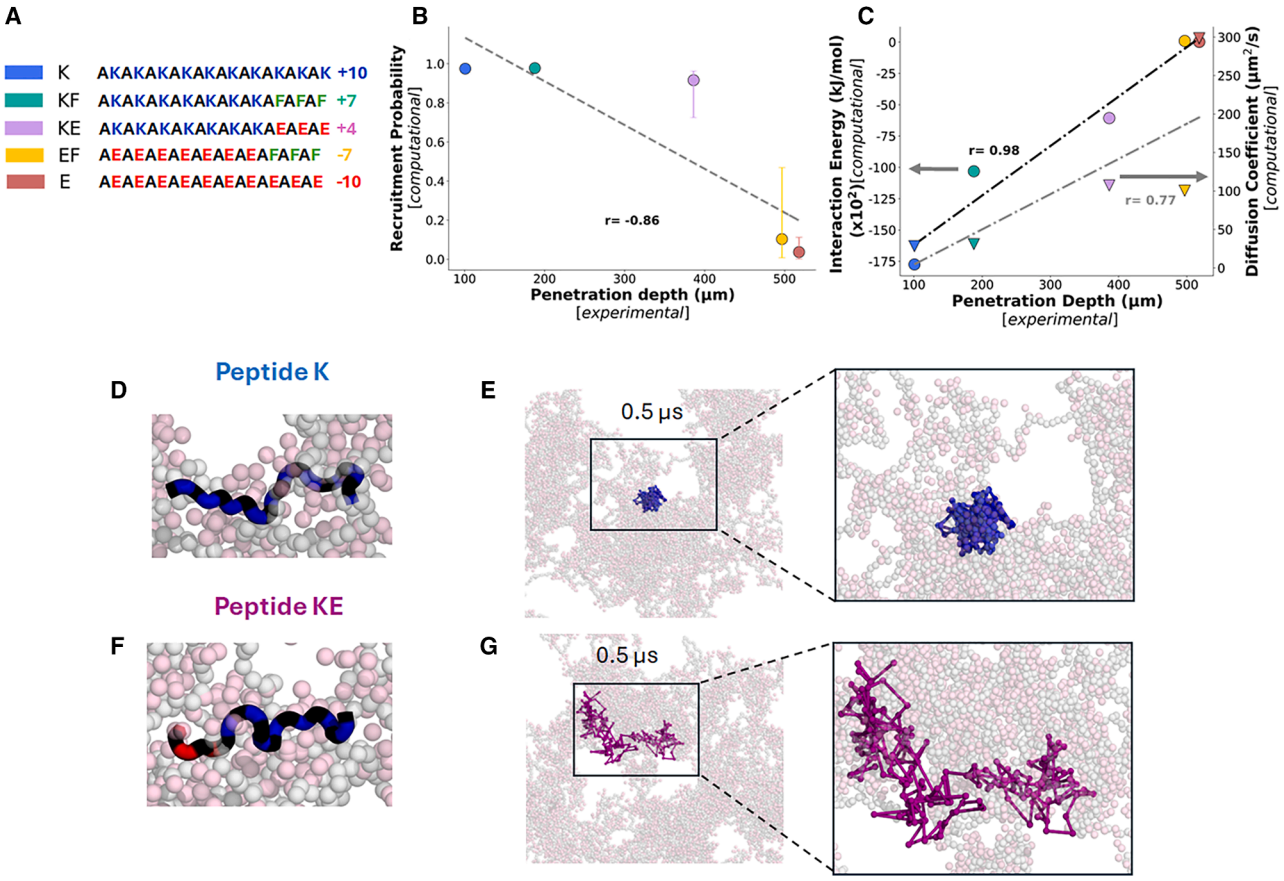

FIGURE 5 Diffusion of peptides through glycosylated PTS regions of mucin. (*A*) Interactions between five different peptides and a preformed glycosylated PTS assembly were studied using the CG model. The sequences of the five peptides (which differ in terms of the numbers of positively charged, negatively charged, and aromatic residues they contain) and their net charge are depicted. (*B*) The correlation between the calculated peptide recruitment probability and the experimental peptide penetration depth for the five peptides in (*A*). Recruitment probability was calculated from simulations of the peptides penetrating PTS polymers that were glycosylated with core-3 glycans to the 40% level. (*C*) Correlations of the electrostatic interaction energies of each the five studied peptides penetrating the glycosylated PTS (left *y* axis) and of their diffusion coefficients (right *y* axis) plotted against the experimentally measured penetration depths. The computational results were obtained as the average of 50 independently diffusing peptides. The experimental values were adopted from (71). (*D* and *E*) Peptides K and KE, respectively, penetrating glycosylated PTS, illustrating their recruitment. (*F* and *G*) Representative trajectories of the positions of the centers of mass of (*F*) a single K peptide and (*G*) a single KE peptide within glycosylated PTS during the last 500 ns of the simulation, with a zoomed-in view on the right.

probability was negatively correlated with the experimentally observed peptide penetration depth, with correlation coefficients of 0.85 for core-1 glycans and 0.93 for core-3 glycans.

As the net positive charge on the peptides increased, their attractive interaction with the negatively charged mucin PTS also increased, resulting in a higher probability of penetration into the mucin matrix, as shown in Figs. 5 *B* and S10 *A*. However, stronger attractive interactions also caused earlier immobilization of the peptides within the polydimethylsiloxane device, preventing further penetration and leading to lower penetration depths. The electrostatic interaction energy calculated from the simulations correlated strongly with the experimentally measured penetration depths, with a correlation coefficient of 0.98 for both types of glycans. To assess the extent of peptide movement during its interactions with the PTS, we calculated the diffusion coefficients of the peptides and plotted them against penetration depth on the right axes of Figs. 5 *C* and S10 *B*. In general, these findings were consistent with the experimental findings and highlighted the effect of net peptide charge on peptide entry into and movement through mucin PTS. These are important findings for the design of therapeutic peptides optimized for effective penetration and movement within mucin environments.

The noticeable differences in the way peptides bearing different net charges diffuse through glycosylated PTS polymer is further highlighted in Fig. 5, *D*–*G*. Fig. 5 *D* shows a representative peptide of type K with a net charge of +10 diffusing within the mucin PTS, while Fig. 5 *F* shows the corresponding simulated diffusion through mucin PTS of a peptide of type KE with a net charge of +4. Fig. 5, *E* and *G* illustrate the motions of the peptide COMs during the final 500 ns of the simulation.

Please cite this article in press as: Biswas and Levy, Ion-mediated effects of glycosylation on the disordered mucin domain: Insights from coarse-grained simulations, Biophysical Journal (2025), https://doi.org/10.1016/j.bpj.2025.07.021

Peptide K, which has a higher positive charge, exhibited very restricted movement within the PTS, whereas the COM of peptide KE covered a larger area, indicating greater mobility. A zoomed-in view of the motions of the COMs of both peptides further emphasizes this difference. These findings are consistent with the experimental observations, suggesting that peptides with higher positive charges interact more strongly with the mucin PTS, which limits their movement. In contrast, peptides with lower positive charges experience weaker electrostatic interactions with the PTS, allowing for more random and extensive movement.

Organization of glycosylated PTS in the multimeric assembly of full-length MUC2 monomers

The experimentally determined atomistic structure of an assembly of N-terminal ordered domains (D1D2D3CysD1) of MUC2 (PDB: 7A5O) and the proposed multimer assembly of eight full-length MUC2 monomers indicated that the ordered domains of MUC2 formed a central filament (Fig. S6, *A* and *B*), whereas their long, disordered PTS regions, and their C-terminal ordered domains remained solvent-exposed and surrounded the central filament (13) (Fig. S6, *A*–*C*). Previous CG modeling of unglycosylated PTS surrounding the central filament suggested that the PTS regions were arranged as a cloud of disordered polymers with a maximum diameter of 100 nm. Here, our goal was to examine the impact of glycosylation (degree and glycan type) on the multimeric assembly of eight such full-length MUC2 monomers and on the organization of the PTS regions surrounding the central head filaments. In this structure, the central beaded filament was position-restrained throughout the simulation, while the C-terminal ordered regions were modeled as large beads with a diameter of 40 Å, based on previous work (13). The organization of the PTS was analyzed by calculating the density of the PTS clouds at various radial distances from the central axis (head filament) and across different polar angles, which was then visualized using a polar density map (Fig. 6).

Representative structures and polar density maps from simulations where the PTS was glycosylated with core-1 glycans at two glycosylation levels (40 and 80%) are presented in Fig. 6. The organization of the PTS was examined under three conditions: no salt, 20 mM NaCl and 10 mM $CaCl_2$. The changes in PTS organization observed in response to changes in salt (cation type and concentration) and glycosylation level (40 or 80%), as shown by the progression in Fig. 6, were consistent with the structures depicted in Fig. 3. In the absence of salt, the PTS was extensively distributed around the axis, whereas in 10 mM $CaCl_2$, the PTS formed a highly compact structure around the axis. The 20 mM NaCl condition resulted in a moderately distributed organization for both degrees of glycosylation. Mapping the polar density (Fig. 6) revealed an unsymmetrical distribution of beads between the left and right hemispheres. In the left hemisphere, in the absence of salt, beads extended up to 40 nm from the center of the axis. Under the 20 mM NaCl condition, most beads were distributed within a 30 nm radius, while in the 10 mM $CaCl_2$ condition, the majority of beads remained within a radial distance of 20 nm for both glycosylation levels. The right hemisphere of the map followed the same trend, but with the beads demonstrating a narrower distribution.

In general, structures glycosylated at 40% of glycosylation sites exhibited a more uniform distribution of beads across all salt conditions, whereas structures glycosylated to the 80% level displayed increased local clustering, forming small, compact regions characterized by high bead density. This behavior can be attributed to the higher number of negative charges present in highly glycosylated systems. In such cases, cations bind simultaneously to multiple negatively charged glycan beads, thus promoting enhanced clustering and compactness. However, whereas positive ions reduce repulsion between negatively charged beads by acting as bridges, residual negative charges or partially screened charges in the system prevent the beads from aggregating into a single large cluster at 80% glycosylation. Instead, the system stabilizes by forming smaller clusters, where local charge neutrality is more effectively achieved, minimizing residual repulsion.

This observation does not depend on whether glycosylation involves core-3 glycans or core-1 glycans, with similar findings for both. The representative structures and polar density maps for simulations of PTS glycosylated with core-3 glycans at two glycosylation levels (40 and 80%) are shown in Fig. S11. Systems glycosylated with core-3 glycans exhibited fewer clustered areas in their structures, such that the overall bead distribution was more uniform compared with those glycosylated with core-1 glycans. The beads in systems with core-3 glycans and 40% glycosylation showed the most uniform distribution, as they had the lowest number of negative charges. In contrast, systems with core-1 glycans and 80% glycosylation exhibited the highest density of compact clusters, as they had the greatest number of negative charges in the system. These findings elucidate the conformational behavior of MUC2 presecretion assemblies under varying glycan and salt conditions.

CONCLUSIONS

In this study, we aimed to investigate how glycosylation and ionic conditions influence the structural properties of secreted intestinal or respiratory mucins, specifically belonging to MUC2, MUC5AC, and MUC5B families, which can be instrumental in explaining rapid volume expansion of secreted mucin upon secretion, as well as, various pathological conditions such as inflammatory bowel disease, cystic fibrosis, and asthma. Our study demonstrates

Please cite this article in press as: Biswas and Levy, Ion-mediated effects of glycosylation on the disordered mucin domain: Insights from coarse-grained simulations, Biophysical Journal (2025), https://doi.org/10.1016/j.bpj.2025.07.021

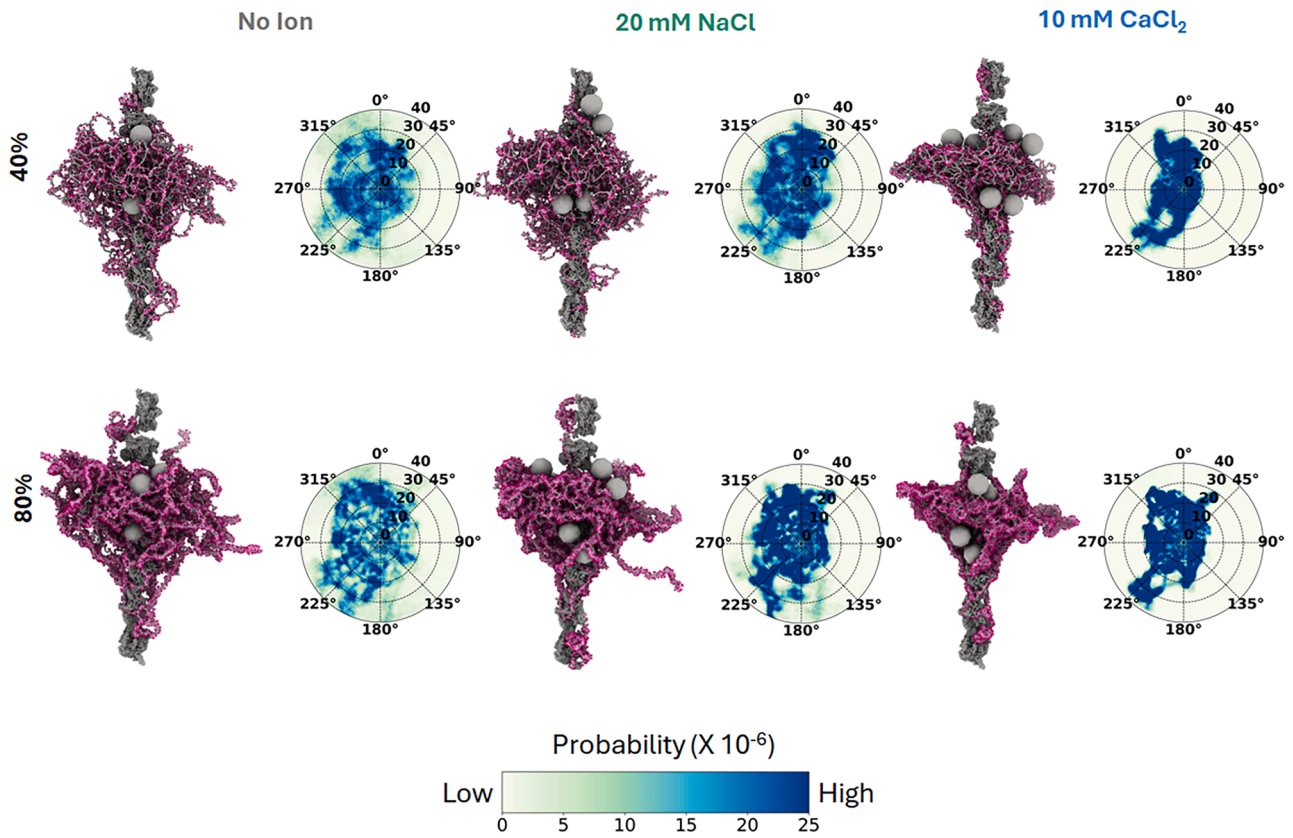

FIGURE 6 Organization of glycosylated disordered PTS in the multimeric assembly of full-length MUC2. Representative simulation structures of the multimeric assembly of eight full-length MUC2 monomers glycosylated with core-1 glycans at 40 and 80% of their glycosylation sites and compared across three salt conditions, as indicated. A polar density map of the PTS beads throughout the simulation is shown to the right of each representative structure. Simulations of duration 500 ns were sampled by taking 500 snapshots, and the atomic positions of all PTS beads in these snapshots were then converted into cylindrical polar coordinates, with the central filament axis serving as the cylindrical coordinate axis. The bead distributions at various angles and distances from the central axis were plotted using a normalization factor, calculated as the total number of beads in each system multiplied by the total number of snapshots. This distribution effectively represents the normalized density of beads surrounding the central axis throughout the simulation (see *color bar* at bottom). The position of the central filament was restrained throughout the simulation and the C-terminal domains were modeled as large beads with a radius of 40 Å.

that the structural organization of glycosylated mucin PTS depends strongly on the properties of the glycan unit as well as on the type and concentration of the cation in solution. In general, divalent salts promote more compact conformations, whereas monovalent salts lead to more expanded ones. For instance, an assembly of four 40% glycosylated PTS chains, each containing 2500 amino acids, undergoes a 34% reduction in R_g when exposed to 20 mM NaCl compared with their dimensions in the absence of salt, whereas in the presence of 10 mM $CaCl_2$, compaction reaches 57% (Fig. 4 *A*). This salt-induced effect is strongly influenced by the number of negatively charged glycans in the system, quantified here by the degree of glycosylation. By contrast, when glycans are attached to 80% of glycosylation sites, the decreases in R_g upon exposure to 20 mM NaCl and 10 mM $CaCl_2$ are 31 and 43%, respectively. The reduction in the size of the PTS molecule upon the addition of monovalent or divalent salts appears to be more pronounced at lower degrees of glycosylation. This can be attributed to the cations shielding the negative charges on the glycans, with a consequent reduction in the strength of inter-glycan electrostatic repulsion leading to an overall compaction of the PTS molecule. The observed salt-induced structural compaction of long PTS chains is relevant to understanding the assembly of MUC2 in the secretion stage. Furthermore, elevated levels of calcium salts, as reported in certain obstructive pulmonary conditions such as cystic fibrosis and asthma (10,25,28,29), may contribute to the formation of more concentrated mucin networks. This could result in a denser molecular mesh than that typically observed under normal physiological conditions, a phenomenon that our findings can help to elucidate.

Interestingly, despite the decreased reduction in R_g at higher degrees of glycosylation, the percentage of glycan charge neutralization upon salt addition is higher at the 80% glycosylation level (19 and 25% for 20 mM NaCl and 10 mM $CaCl_2$, respectively) compared with the 40% glycosylation level (9 and 20% for 20 mM NaCl and

Please cite this article in press as: Biswas and Levy, Ion-mediated effects of glycosylation on the disordered mucin domain: Insights from coarse-grained simulations, Biophysical Journal (2025), https://doi.org/10.1016/j.bpj.2025.07.021

10 mM $CaCl_2$, respectively) (Fig. 4 *B*). This observation likely arises from the presence of a higher charge density at greater glycosylation levels, which allows single cations to neutralize multiple charges. Both higher charge neutralization and increased electrostatic repulsion at higher degrees of glycosylation contribute to the formation of more local clustering and localized substructures within the PTS assembly, despite an overall expansion in the molecular radius. Reduced glycosylation and the presence of smaller glycans have been associated with ulcerative colitis and inflammatory bowel disease, both characterized by chronic inflammation. Our findings suggest that lower levels of glycosylation reduce the shielding provided by sugar moieties, potentially weakening the mucosal protective barrier formed by mucin molecules against inflammatory triggers.

To explore the effect of the charge on each individual glycan chain on PTS structural organization, we analyzed two glycan types: mono-sialylated core-3 glycans, bearing a single negative charge per chain; and di-sialylated core-1 glycans, bearing two negative charges per chain. Across all salt types and glycosylation levels, the extent of R_g reduction and charge neutralization was lower for core-3 glycans compared with core-1 glycans. For instance, at 40% glycosylation, the reduction in Rg for core-3 glycans was 21% in the presence of 20 mM NaCl and 39% in the presence of 10 mM $CaCl_2$ (Fig. S8 *B*) (with corresponding values of 34 and 57%, respectively, with core-1 glycans, Fig. 4 *A*). This is likely because the lower charge on individual mono-sialylated core-3 glycans reduces the likelihood of glycan-cation interactions, resulting in greater conformational variability in a polymer bearing core-3 glycans compared with core-1 glycans.

In addition to studying the structural arrangement of long PTS chains to better understand the assembly of MUC2 in the secretion stage, we also studied the structural organization of PTS in the presecreted stage by simulating the assembly of a multimer comprising eight full-length MUC2 monomers (using PDB: 7A5O). Similarly to PTS in the secreted stage, the compaction of the PTS domain in the presecreted stage is more strongly affected by the presence of $CaCl_2$ compared with NaCl, and it forms localized clusters at higher glycan charge densities. We showed that the dense organization of the disordered glycosylated PTS permits recruitment of peptides that can diffuse within the networks of interacting PTS chains. Our observations align qualitatively with experimental findings (71) showing that peptide penetration depth and diffusion are strongly influenced by peptide charge content.

Taken together, our investigations into both secreted mucin and presecretion assemblies provide a molecular understanding of the possible conformational states of MUC2 throughout the mucin secretion pathway. Although MUC2 forms polymers in both the secreted and presecretion stages, the organization of these polymers differs significantly before and after secretion. Within the Golgi, the multimer assembly of MUC2 remains in a highly condensed phase, possibly due to the action of Ca^{2+} ions, as depicted in Fig. 7 *A*. During secretion, when the vesicle opens, Ca^{2+} ions begin to be replaced by Na^+ ions, leading to a more expanded conformation. This transitional state is represented by Fig. 7 *B*, where some Ca^{2+} ions are displaced, but the overall multimer assembly remains intact. Following secretion and the dissociation of the D1 and D2 domains, the mucin monomers organize themselves into the head-to-head, tail-to-tail secretion assembly. In this study, the secreted mucin structure was modeled in a simplified manner, excluding the ordered mucin domains that are naturally present in the secretion assembly. Nonetheless, we found that, during the formation of the secretion assembly, many Ca^{2+} ions remain embedded within the mucin matrix, as represented by Fig. 7 *C*. Finally, when most of the Ca^{2+} ions are replaced by Na^+ ions, the system transitions to the state depicted in Fig. 7 *D*.

The CG model presented in this study is designed to capture residue-level conformational changes of mucin PTS domains at the tens-of-nanometer length scale; however, the insights gained from these simulations can inform hypotheses regarding the larger-scale organization and behavior of mucus networks at micron-scale resolutions. Overall, this study provides a detailed molecular picture of mucin PTS assembly during secretion, offering valuable insights into the structural and functional dynamics of mucin. By quantifying mucin chain compaction under varying ionic and glycosylation conditions, our model offers insight into the physical determinants of mucus mesh density, which in turn influences barrier permeability, hydration retention, and pathogen exclusion—key functional aspects of the mucus barrier. Extending this model

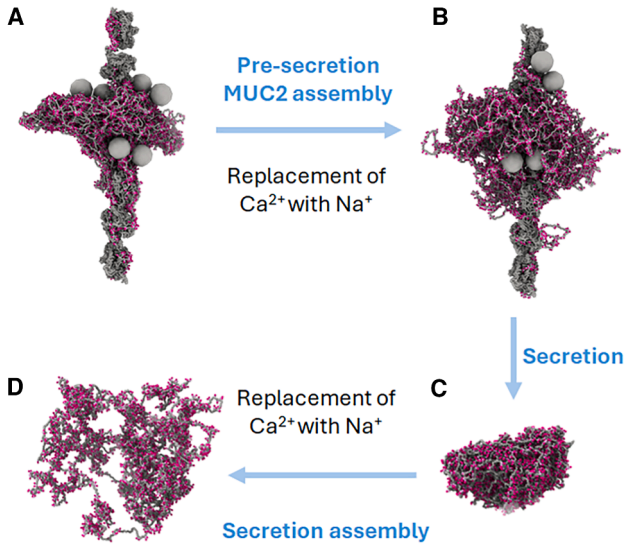

FIGURE 7 Possible conformational states in the MUC2 secretion pathway. Upper panels: structures representing the possible presecretion assembly of MUC2 glycosylated with core-1 glycan at 40% of its glycosylation sites under conditions of (*A*) 10 mM $CaCl_2$ and (*B*) 20 mM NaCl. Lower panels: structures representing the possible secretion assembly of MUC2 glycosylated with core-1 glycan at 40% of its glycosylation sites under conditions of (*C*) 10 mM $CaCl_2$ and (*D*) 20 mM NaCl.

Please cite this article in press as: Biswas and Levy, Ion-mediated effects of glycosylation on the disordered mucin domain: Insights from coarse-grained simulations, Biophysical Journal (2025), https://doi.org/10.1016/j.bpj.2025.07.021

to larger assemblies will enable quantitative predictions of key mucus barrier properties such as viscoelasticity and porosity. Moreover, incorporating glycan compositions specific to healthy and diseased conditions is essential to better understand mucin function.

ACKNOWLEDGMENTS

Y.L. holds the Morton and Gladys Pickman professional chair in Structural Biology.

Y.L. is grateful for support from the Israel Science Foundation (grant no. 2072/22), a research grant from the Estate of Gerald Alexander, and a research grant from the Donald Gordon Foundation.

AUTHOR CONTRIBUTIONS

G.B. performed simulations and analysis. G.B. and Y.L. designed the project and wrote the manuscript.

DECLARATION OF INTERESTS

The authors declare no competing interests.

SUPPORTING MATERIAL

Supporting material can be found online at https://doi.org/10.1016/j.bpj.2025.07.021.

REFERENCES

1. Wagner, C. E., K. M. Wheeler, and K. Ribbeck. 2018. Mucins and Their Role in Shaping the Functions of Mucus Barriers. *Annu. Rev. Cell Dev. Biol.* 34:189–215.
2. Mcshane, A., J. Bath, …, K. Ribbeck. 2021. Mucus. *Curr. Biol.* 31: R938–R945.
3. Bansil, R., and B. S. Turner. 2006. Mucin structure, aggregation, physiological functions and biomedical applications. *Curr. Opin. Colloid Interface Sci.* 11:164–170.
4. Bansil, R., and B. S. Turner. 2018. The biology of mucus: Composition, synthesis and organization. *Adv. Drug Deliv. Rev.* 124:3–15.
5. Song, D., D. Cahn, and G. A. Duncan. 2020. Mucin biopolymers and their barrier function at airway surfaces. *Langmuir.* 36:12773–12783.
6. Corfield, A. P. 2015. Mucins: A biologically relevant glycan barrier in mucosal protection. *Biochim. Biophys. Acta.* 1850:236–252.
7. Fass, D., and D. J. Thornton. 2023. Mucin networks: Dynamic structural assemblies controlling mucus function. *Curr. Opin. Struct. Biol.* 79:102524.
8. Vinall, L. E., A. S. Hill, …, D. M. Swallow. 1998. Variable number tandem repeat polymorphism of the mucin genes located in the complex on 11p15.5. *Hum. Genet.* 102:357–366.
9. Hattrup, C. L., and S. J. Gendler. 2008. Structure and function of the cell surface (tethered) mucins. *Annu. Rev. Physiol.* 70:431–457.
10. Verdugo, P. 2012. Supramolecular dynamics of mucus. *Cold Spring Harb. Perspect. Med.* 2:a009597.
11. Weston, A., S. C. Vladescu, …, G. H. Carpenter. 2023. The influence of ions on the lubricative abilities of mucin and the role of sialic acids. *Colloids Surf. B Biointerfaces.* 227:113327.
12. Thornton, D. J., K. Rousseau, and M. A. McGuckin. 2008. Structure and function of the polymeric mucins in airways mucus. *Annu. Rev. Physiol.* 70:459–486.
13. Javitt, G., L. Khmelnitsky, …, D. Fass. 2020. Assembly Mechanism of Mucin and von Willebrand Factor Polymers. *Cell.* 183:717–729.e16.
14. Ambort, D., M. E. V. Johansson, …, G. C. Hansson. 2012. Perspectives on mucus properties and formation-lessons from the biochemical world. *Cold Spring Harb. Perspect. Med.* 2:a014159.
15. A, V., R. D. C, …, S. PH. 2015. Essentials of Glycobiology, 4th Edition. Cold Spring Harbor Laboratory Press.
16. Verdugo, P. 1990. Goblet cells secretion and mucogenesis. *Annu. Rev. Physiol.* 52:157–176.
17. Chin, W. C., I. Quezada, …, P. Verdugo. 2005. Modeling Ca-polyanion crosslinking in secretory networks. Assessment of charge density and bond affinity in polyanionic secretory networks. *Macromol. Symp.* 227:89–96.
18. Hughes, G. W., C. Ridley, …, D. J. Thornton. 2019. The MUC5B mucin polymer is dominated by repeating structural motifs and its topology is regulated by calcium and pH. *Sci. Rep.* 9:17350.
19. Tam, P. Y., and P. Verdugo. 1981. Control of mucus hydration as a Donnan equilibrium process. *Nature.* 292:340–342.
20. Espinosa, M., G. Noé, …, M. Villalón. 2002. Acidic pH and increasing [Ca2+] reduce the swelling of mucins in primary cultures of human cervical cells. *Hum. Reprod.* 17:1964–1972.
21. Raynal, B. D. E., T. E. Hardingham, …, D. J. Thornton. 2003. Calcium-dependent protein interactions in MUC5B provide reversible cross-links in salivary mucus. *J. Biol. Chem.* 278:28703–28710.
22. Crowther, R. S., and C. Marriott. 1984. Counter-ion binding to mucus glycoproteins. *J. Pharm. Pharmacol.* 36:21–26.
23. Cantero-Recasens, G., C. M. Butnaru, …, V. Malhotra. 2019. Sodium channel TRPM4 and sodium/calcium exchangers (NCX) cooperate in the control of Ca2-induced mucin secretion from goblet cells. *J. Biol. Chem.* 294:816–826.
24. Su, Y., Y. Xu, …, J. Wu. 2009. Spectroscopic studies of the effect of the metal ions on the structure of mucin. *J. Mol. Struct.* 920:8–13.
25. Forstner, J. F., and G. G. Forstner. 1976. Effects of calcium on intestinal mucin: implications for cystic fibrosis. *Pediatr. Res.* 10:609–613.
26. Yan, H., C. Chircov, …, T. Crouzier. 2018. Reversible Condensation of Mucins into Nanoparticles. *Langmuir.* 34:13615–13625.
27. Wagner, C. E., B. S. Turner, …, K. Ribbeck. 2017. A Rheological Study of the Association and Dynamics of MUC5AC Gels. *Biomacromolecules.* 18:3654–3664.
28. Chen, E. Y. T., N. Yang, …, W. C. Chin. 2010. A new role for bicarbonate in mucus formation. *Am. J. Physiol. Lung Cell. Mol. Physiol.* 299:1542–L549.
29. Morrison, C. B., M. R. Markovetz, and C. Ehre. 2019. Mucus, mucins, and cystic fibrosis. *Pediatr. Pulmonol.* 54:S84–S96.
30. Marczynski, M., B. N. Balzer, …, O. Lieleg. 2020. Charged glycan residues critically contribute to the adsorption and lubricity of mucins. *Colloids Surf. B Biointerfaces.* 187:110614.
31. An, J., C. Jin, …, P. M. Claesson. 2017. Influence of Glycosylation on Interfacial Properties of Recombinant Mucins: Adsorption, Surface Forces, and Friction. *Langmuir.* 33:4386–4395.
32. Larsson, J. M. H., H. Karlsson, …, G. C. Hansson. 2011. Altered O-glycosylation profile of MUC2 mucin occurs in active ulcerative colitis and is associated with increased inflammation. *Inflamm. Bowel Dis.* 17:2299–2307.
33. Theodoratou, E., H. Campbell, …, G. Lauc. 2014. The role of glycosylation in IBD. *Nat. Rev. Gastroenterol. Hepatol.* 11:588–600.
34. Shirazi, T., R. J. Longman, …, C. S. Probert. 2000. Mucins and inflammatory bowel disease. *Postgrad. Med. J.* 76:473–478.
35. Hayes, C. A., S. Nemes, and N. G. Karlsson. 2012. Statistical analysis of glycosylation profiles to compare tissue type and inflammatory disease state. *Bioinformatics.* 28:1669–1676.
36. Zhang, Y., L. Sun, …, Y. Zhang. 2022. A Sweet Warning: Mucin-Type O-Glycans in Cancer. *Cells.* 11:3666.

37. Du, J., B. M. Nagda, …, A. L. Fogelson. 2023. A computational framework for the swelling dynamics of mucin-like polyelectrolyte gels. *J. Nonnewton. Fluid Mech.* 313:104989.

38. Sircar, S., J. P. Keener, and A. L. Fogelson. 2013. The effect of divalent vs. monovalent ions on the swelling of Mucin-like polyelectrolyte gels: Governing equations and equilibrium analysis. *J. Chem. Phys.* 138:014901.

39. Gniewek, P., and A. Kolinski. 2012. Coarse-Grained Modeling of Mucus Barrier Properties. *Biophys. J.* 102:195–200.

40. Wang, J., and X. Shi. 2017. Molecular dynamics simulation of diffusion of nanoparticles in mucus. *Acta Mech. Solida Sin.* 30:241–247.

41. Gniewek, P., and A. Kolinski. 2010. Coarse-Grained Monte Carlo Simulations of Mucus : Structure, Dynamics, and Thermodynamics. *Biophys. J.* 99:3507–3516.

42. Ford, A. G., X. Z. Cao, …, M. G. Forest. 2021. Molecular dynamics simulations to explore the structure and rheological properties of normal and hyperconcentrated airway mucus. *Stud. Appl. Math.* 147:1369–1387.

43. Rubinstein, A., L. Kinarsky, and S. Sherman. 2004. Molecular Dynamics Simulations of the O-glycosylated 21-residue MUC1 Peptides. *Int. J. Mol. Sci.* 5:119–128.

44. Kearns, F. L., M. A. Rosenfeld, and R. E. Amaro. 2024. Breaking Down the Bottlebrush: Atomically-Detailed Structural Dynamics of Mucins. *J. Chem. Inf. Model.* 64:7949–7965.

45. Forstner, J. F., and G. G. Forstner. 1975. Calcium Binding to Intestinal Goblet Cell Mucin. *Biochim. Biophys. Acta.* 386:283–292.

46. Ambort, D., M. E. V. Johansson, …, G. C. Hansson. 2012. Calcium and pH-dependent packing and release of the gel-forming MUC2 mucin. *Proc. Natl. Acad. Sci. USA.* 109:5645–5650.

47. Feldötö, Z., T. Pettersson, and A. Dedinaite. 2008. Mucin - Electrolyte Interactions at the Solid - Liquid Interface Probed by QCM-D. *Langmuir.* 24:3348–3357.

48. Cao, X., R. Bansil, …, N. H. Afdhal. 1999. pH-dependent conformational change of gastric mucin leads to sol-gel transition. *Biophys. J.* 76:1250–1258.

49. Sun, L., Y. Zhang, …, Y. Zhang. 2023. Mucin Glycans: A Target for Cancer Therapy. *Molecules.* 28:7033.

50. Capon, C., E. Maes, …, Y. S. Kim. 2001. Sda-antigen-like structures carried on core 3 are prominent features of glycans from the mucin of normal human descending colon. *Biochem. J.* 358:657–664.

51. Dall'olio, F., M. Pucci, and N. Malagolini. 2021. The cancer-associated antigens sialyl lewisa/x and sda: Two opposite faces of terminal glycosylation. *Cancers (Basel).* 13:5273.

52. Bateman, A., M. J. Martin, …, D. Teodoro. 2021. UniProt: the universal protein knowledgebase in 2021. *Nucleic Acids Res.* 49:D480–D489.

53. PyMOL. The PyMOL Molecular Graphics System, Version. 2.5 Schrödinger, LLC.

54. Park, S. J., J. Lee, …, W. Im. 2019. CHARMM-GUI Glycan Modeler for modeling and simulation of carbohydrates and glycoconjugates. *Glycobiology.* 29:320–331.

55. Huang, J., and A. D. Mackerell. 2013. CHARMM36 all-atom additive protein force field: Validation based on comparison to NMR data. *J. Comput. Chem.* 34:2135–2145.

56. Shental-bechor, D., and Y. Levy. 2008. Effect of glycosylation on protein folding : A close look at thermodynamic stabilization. *Proc. Natl. Acad. Sci. USA.* 105:8256–8261.

57. Clementi, C., H. Nymeyer, and J. N. Onuchic. 2000. Topological and energetic factors: What determines the structural details of the transition state ensemble and "en-route" intermediates for protein folding? An investigation for small globular proteins. *J. Mol. Biol.* 298:937–953.

58. Guvench, O., S. S. Mallajosyula, …, A. D. Mackerell. 2011. CHARMM additive all-Atom force field for carbohydrate derivatives and its utility in polysaccharide and carbohydrate–protein modeling. *J. Chem. Theory Comput.* 7:3162–3180.

59. Hazra, M. K., Y. Gilron, and Y. Levy. 2023. Not Only Expansion : Proline Content and Density Also Induce Disordered Protein Conformation Compaction. *J. Mol. Biol.* 435:168196.

60. Malmberg, C. G., and A. A. Maryott. 1956. Dielectric constant of water from 0 to 100 C. *J. Res. Natl. Bur. Stand. (U.S.).* 1934:56.

61. Noel, J. K., M. Levi, …, P. C. Whitford. 2016. SMOG 2: A Versatile Software Package for Generating Structure-Based Models. *PLoS Comput. Biol.* 12:e1004794–14.

62. Allen, M. P., and D. J. Tildesley. 2017. Computer Simulation of Liquids, Second edition. Oxford University Press.

63. Hansen, J. P., and I. R. McDonald. 2013. Theory of Simple Liquids: With Applications to Soft Matter, Fourth Edition. Academic Press.

64. Joseph, J. A., A. Reinhardt, …, R. Collepardo-Guevara. 2021. Physics-driven coarse-grained model for biomolecular phase separation with near-quantitative accuracy. *Nat. Comput. Sci.* 1:732–743.

65. Jo, S., T. Kim, …, W. Im. 2008. CHARMM-GUI: A web-based graphical user interface for CHARMM. *J. Comput. Chem.* 29:1859–1865.

66. Jorgensen, W. L., J. Chandrasekhar, …, M. L. Klein. 1983. Comparison of simple potential functions for simulating liquid water. *J. Chem. Phys.* 79:926–935.

67. Abraham, M. J., T. Murtola, …, E. Lindahl. 2015. Gromacs: High performance molecular simulations through multi-level parallelism from laptops to supercomputers. *SoftwareX.* 1–2:19–25.

68. Lin, X., and B. Zhang. 2024. Explicit ion modeling predicts physicochemical interactions for chromatin organization. *eLife.* 12:RP90073.

69. Freeman, G. S., D. M. Hinckley, and J. J. De Pablo. 2011. A coarse-grain three-site-per-nucleotide model for DNA with explicit ions. *J. Chem. Phys.* 135:165104.

70. Bacle, P., M. Jardat, …, V. Dahirel. 2020. Coarse-Grained Models of Aqueous Solutions of Polyelectrolytes: Significance of Explicit Charges. *J. Phys. Chem. B.* 124:288–301.

71. Samad, T., J. Witten, …, K. Ribbeck. 2022. Spatial configuration of charge and hydrophobicity tune particle transport through mucus. *Biophys. J.* 121:277–287.

72. Urry, D. W. 1997. Physical chemistry of biological free energy transduction as demonstrated by elastic protein-based polymers. *J. Phys. Chem. B.* 101:11007–11028.

73. Carl, N., S. Prévost, …, K. Huber. 2019. Invertible Micelles Based on Ion-Specific Interactions of Sr2+ and Ba2+ with Double Anionic Block Copolyelectrolytes. *Macromolecules.* 52:8759–8770.

74. Crater, J. S., and R. L. Carrier. 2010. Barrier Properties of Gastrointestinal Mucus to Nanoparticle Transport. *Macromol. Biosci.* 10:1473–1483.

75. Lieleg, O., I. Vladescu, and K. Ribbeck. 2010. Characterization of particle translocation through mucin hydrogels. *Biophys. J.* 98:1782–1789.

76. Schuster, B. S., J. S. Suk, …, J. Hanes. 2013. Nanoparticle diffusion in respiratory mucus from humans without lung disease. *Biomaterials.* 34:3439–3446.

77. Lai, S. K., D. E. O'Hanlon, …, J. Hanes. 2007. Rapid transport of large polymeric nanoparticles in fresh undiluted human mucus. *Proc. Natl. Acad. Sci. USA.* 104:1482–1487.

78. Li, L. D., T. Crouzier, …, K. Ribbeck. 2013. Spatial configuration and composition of charge modulates transport into a mucin hydrogel barrier. *Biophys. J.* 105:1357–1365.

79. Wenzler, A., and O. Lieleg. 2018. Transient binding promotes molecule penetration into mucin hydrogels by enhancing molecular partitioning. *Biomater. Sci.* 6:3373–3387.